ECS Journal of Solid State
Science and Technology

The Electrochemical Society
Advancing solid state & electrochemical science & technology

OPEN ACCESS

Void Formation Mechanism Related to Particles During Wafer-to-Wafer Direct Bonding

To cite this article: F. Nagano *et al* 2022 *ECS J. Solid State Sci. Technol.* **11** 063012

View the article online for updates and enhancements.

Investigate your battery materials under defined force!
The new PAT-Cell-Force, especially suitable for solid-state electrolytes!

- Battery test cell for force adjustment and measurement,
  0 to 1500 Newton (0-5.9 MPa at 18mm electrode diameter)
- Additional monitoring of gas pressure and temperature

www.el-cell.com +49 (0) 40 79012 737 sales@el-cell.com

EL-CELL®
electrochemical test equipment

This content was downloaded from IP address 91.181.237.252 on 30/06/2022 at 15:17

ECS Journal of Solid State Science and Technology, 2022 **11** 063012

Void Formation Mechanism Related to Particles During Wafer-to-Wafer Direct Bonding

F. Nagano,[1,2,z] S. Iacovo,[2] A. Phommahaxay,[2] F. Inoue,[2,a] F. Chancerel,[2] H. Naser,[2] G. Beyer,[2] E. Beyne,[2,*] and S. De. Gendt[1,2]

[1]*Department of Chemistry, KU Leuven, Celestijnenlaan 200 f, 3001 Leuven, Belgium*
[2]*imec, Kapeldreef 75, 3001 Leuven, Belgium*

Achieving a void-free bonding interface is an important requirement for the wafer-to-wafer direct bonding process. The two main potential mechanisms for void formation at the interface are (i) void formation induced by gas, such as condensation by-products caused by the bonding process or outgassing of trapped precursors, and (ii) void formation induced by physical obstacles, such as particles. In this work, emphasis is on the latter process. Particles were intentionally deposited on the wafer prior to bonding to study the kinetics of the physical void formation process. Void formations induced by particles deposited on different dielectrics bonding materials were analyzed using scanning acoustic microscopy and image software. The void formation mechanism is then discussed along with the wafer bonding dynamics at room temperature.
© 2022 The Author(s). Published on behalf of The Electrochemical Society by IOP Publishing Limited. This is an open access article distributed under the terms of the Creative Commons Attribution 4.0 License (CC BY, http://creativecommons.org/licenses/by/4.0/), which permits unrestricted reuse of the work in any medium, provided the original work is properly cited. [DOI: 10.1149/2162-8777/ac7662]

Manuscript submitted December 23, 2021; revised manuscript received May 29, 2022. Published June 16, 2022.

Supplementary material for this article is available online

Three-dimensional (3D) circuit integration is a promising technology to overcome the limitation of conventional two-dimensional (2D) scaling. Several techniques allow the construction of circuits in a vertical manner, at the wafer-level or the die-level. These are either based on 3D sequential or monolithic integration requiring solder base micro bump interconnects and TSV's (Through Silicon Via).[1–7] Wafer-to-wafer direct hybrid bonding has recently been raised as one attractive stacking scheme enabling finer pitch interconnection, high-accuracy integration, and lower production cost. Direct bonding can now be performed at room temperature on a full wafer-level, because of the combination of the ultra-smooth surface obtained by chemical mechanical polishing (CMP) and the plasma activated dielectric surface.[8–15] Also, a wafer-to-wafer hybrid bonding scheme has been developed for specific applications, such as 3D system-on-chip (3D-SOC) solutions and high-end complementary metal oxide semiconductor (CMOS) image sensors. Hybrid bonding requires both direct bonding of dielectric-to-dielectric and Cu-to-Cu sub-micron pad in one processing step. In the latter, the Cu pad is slightly recessed on the top wafer and protruded on the bottom wafer following a novel CMP process.[16,17] In general, to cope with the 3D circuit integration, wafer-to-wafer direct bonding must achieve three conditions: high bonding energy of the dielectric materials' bonding interface (> 1.7 J m^{-2}) to survive mechanical processes, such as grinding and dicing,[18] low-temperature processing (< 450 °C), and no unbonded area, e.g., void formation, on the full wafer area. Since in general for hybrid bonding schemes the area of dielectric layer occupies over 75% of a 300 mm patterned wafer, the bonding quality is mostly relying on the direct bonding of the dielectric layer. Therefore, the direct bonding mechanism of the dielectric layer, SiO_2 for example, has been studied fundamentally over the years,[18–24] leading to improved bonding quality. In our previous work, instead of the usual SiO_2, we showed that SiCN is a promising dielectric because it possesses essential properties, including high bonding energy (~ 2.2 J m^{-2}) at lower annealing temperature conditions (< 250 °C) compared with other dielectrics.[25,11,15,18,2511, 15, 18, 25, 26]

Unbonded areas, also called voids, form at the interface between the two bonding layers and represent a severe problem for wafer-to-wafer direct bonding, as they lead to the loss of electric yield or delamination during subsequent processing steps. Thus, studies of void formation are of great interest to further optimize the bonding process. There are two potential schemes for void formation at the interface: (i) chemical voids, related to gaseous by-products formed during the bonding condensation reaction or precursor outgassing from the dielectrics,[18,27] or (ii) physical voids related to formation induced by physical factors, such as surface curvature, asperities, trapped and remained air by bond wave propagation, and particles.[28–31] In the case of physical obstacles remaining on the bonding surface, the void formation occurs during the bonding process, regardless of the bonding dielectric, whereas chemical voids are strongly related to the chemical nature and pre-processing of the bonding dielectrics.[28–30] In the latter work, the authors debonded a particle containing wafer and observed compression of the original particle. In our work we observe a similar compression for the polymer particles, but we believe that this effect is minimal for the W particles, due to the hardness of the latter. The actual particle contamination issue has been recognized to be, for example, the organic residues of resist material from the stripping process and Si debris produced during the dicing or edge trimming process. These Si debris are generally 100 nm to few micrometres size, expecting micro level void formation. Due to manufacturing considerations of artificial particles, one has to assume that the radius circumscribes the shape of experimentally observed random shapes. For SiCN, no/limited outgassing, e.g., chemical voids, were observed even if the post bond annealing of SiCN was performed at temperatures higher than the dielectric deposition temperature. One specific case of physical voids formation originates from misalignment of patterned wafers during bonding, i.e., the protruding Cu pad lands on the dielectric surface, forming a physical obstacle. To reduce these physical voids, bonding schemes should be developed to improve the bonding overlay accuracy which could also lead to narrower pitch. Another case of physical voids originates from external physical obstacles laying on the wafer area. In this work, we aim to understand the void formation induced by these physical obstacles. Therefore, physical voids are intentionally induced by depositing particles of various nature and dimensions on selected dielectrics and various techniques are deployed to characterize the physical void formation. Finally, the correlation between the type of particles and physical void formation is elucidated, thus allowing future optimization of the wafer-to-wafer direct bonding at room temperature. On the other hand, in past studies it has been reported

*Electrochemical Society Member.
[a]Present address: Faculty of Engineering, Yokohama National University, 79–5 Tokiwadai, Hodogaya, Yokohama 240–8501, Japan
[z]E-mail: Fuya.Nagano@imec.be

that the bond wave during wafer bonding is also one of key factors that create the physical voids at the bonding interface[32,33] As the bond wave propagation can be impacted by particles deposited on the wafer surface, the correlation between the particle and the bond wave propagation is also discussed in this paper.

Experimental

Sample preparation and process flow.—In this study, 300 mm Si (100) p-type wafers were prepared for wafer bonding experiments. SiCN was deposited on the substrate by plasma enhanced chemical vapor deposition (PECVD) at 370 °C. The film thickness target after deposition was 120 nm and verified by Spectroscopic Ellipsometry (F5-SCD, KLA-Tencor). All wafers were then annealed in 10% H_2/N_2 atmosphere at 400 °C for 10 min after the deposition. After post-deposition annealing, the film surface was smoothened by a CMP process with relevant barrier metal slurry and pad. The thickness for SiCN film was reduced to 93 nm after CMP. The arithmetic average of the roughness profile, R_a was determined on a scan field of 500 nm × 500 nm by atomic force microscope (AFM; NX3DM, Park Systems) after the PDA and CMP. Figure 1 shows the AFM images of SiCN surface after PDA and CMP. A smooth surface was obtained, with an arithmetic average of the roughness profile R_a of 0.08 nm for SiCN after CMP, allowing direct bonding (Fig. 1a). This atomic-level smoothness of SiCN surface has been achieved for the hybrid bonding scheme in our past work too.[11,25] The surface roughness after N_2 plasma activation was obtained as a similar R_a value of 0.09 nm.

After the CMP process, particle deposition was performed on the bottom wafer dielectric layers. Two kinds of particles with different hardness were selected: a softer polymer material, and harder tungsten (W) particle material. Particles were positioned on the bottom wafer in a 20 × 20 mm grid after the cleaning process (Figs. S1 and S2 (available online at stacks.iop.org/JSS/11/063012/mmedia)). Polymer particles were defined in a controlled manner using a photo-patternable polymer, and W particles were deposited by ion beam in a FIB tool (Expida 1285, FEI). The particle diameter was fixed to 25 μm, and the targeted thickness was 2.6 μm for polymer particles and 2.0 μm for the W particles. The thickness difference was introduced because of the possible shrinkage of polymer due to the force applied by the wafers during bond wave propagation. Figure 2 shows SEM images of polymer and W particles with 25 μm diameters deposited on the bottom wafer. The measured particle dimensions are close to the defined targets. Subsequently, N_2 plasma activation was performed to activate the wafer surface using the EVG GEMINI system and the surface was rinsed with deionized water. Bottom wafers were then bonded with a blanket top wafer (SiCN layer after CMP but without particles) at room temperature and without any specific bonding pressure employed using the EVG GEMINI bonding system. After bonding, the void formation at the bonding interface was inspected using in-line scanning acoustic microscopy (SAM; PVA Tepla AW-SAM300). The maximum peak value of the reflect signal from the bonding interface is targeted to obtain the scanned image. The local change in the total thickness of the bonded wafer pair due to the particles' presence was also investigated using patterned wafer geometry (PWG; KLA). The bonded wafers finally received a post-bond annealing (PBA) at 250 °C for 2 h under ambient N_2 in a furnace (performed in an A412 reactor, ASM) and the void size evolution was investigated a second time using in-line SAM. FTIR analysis on the particle void including the polymer and W particle was performed to compare the components in the polymer particle and W particle void before and after PBA.

Bonding energy characterization.—Here, it is worth noting that the direct bonding can be defined and characterized by two energies as described in the literature.[34,35] The first one is the adherence energy, which is defined as the energy needed to separate one bonded interface into two surfaces (described as G_c in this study). This adherence energy is widely referred to as bonding energy in many articles to characterize the direct bonding.[36–41] It is usually determined using the Maszara test, which involves inserting a razor blade in between the two bonded wafers. The razor blade creates a crack propagating to a certain distance, and this distance can be used to calculate the bonding energy. The general formula to calculate the bonding energy, G_c, can be written as Eq. 1,

$$G_c = \frac{3}{8}\frac{E_{w1}E_{w2}{t_{w1}}^3{t_{w2}}^3}{E_{w1}{t_{w1}}^3 + E_{w2}{t_{w2}}^3}\cdot\frac{{t_b}^2}{{L_c}^4} \quad [1]$$

where G_c is the bonding energy in mJ mm^{-2}, t_b is the blade thickness in mm, E_{w1} and E_{w2} are the Young's modulus of wafer 1 and 2 in Pa, t_{w1} and t_{w2} are the thickness in mm, L_c is the crack length in mm. In this study, identical wafers are used for the bonding. Hence, the formula can be simplified as:

$$G_c = \frac{3E_w{t_w}^3{t_b}^2}{16{L_c}^4} \quad [2]$$

The crack length L_c was measured with a ruler on an IR camera image just after 5 s when first crack stop. Bonding energy was calculated using the blade insertion method after the room temperature bonding and post-bond annealing (PBA) in the controlled air ambient of the clean room which has a constant temperature of 22 °C and relative humidity of 40%.

The second energy describing bonding is the adhesion energy, G_a, the energy that drives the bond wave frontward and close the gap. Turner et al.[34] has reported that G_c and G_a are asymmetrical as the mechanism of adhesion and separation is different and they must be measured differently; usually G_c is higher than $G_a$under the clean room ambient (40% relative humidity). The adhesion energy is usually measured using measurement using an opposite configuration compared to the Maszara test.[35] The razor blade is inserted at the edge of the wafer before two wafers are bonded, when the bonding wave reaches a position close to the inserted blade it is stopped. The adhesion energy is then measured by the length of the unbonded area derived as L_a with same formula used in Maszara test. On the other hand, Rieutord et al. have defined the analytical model between the adhesion energy and the bond wave velocity which allows to calculate the adhesion energy from the bond wave

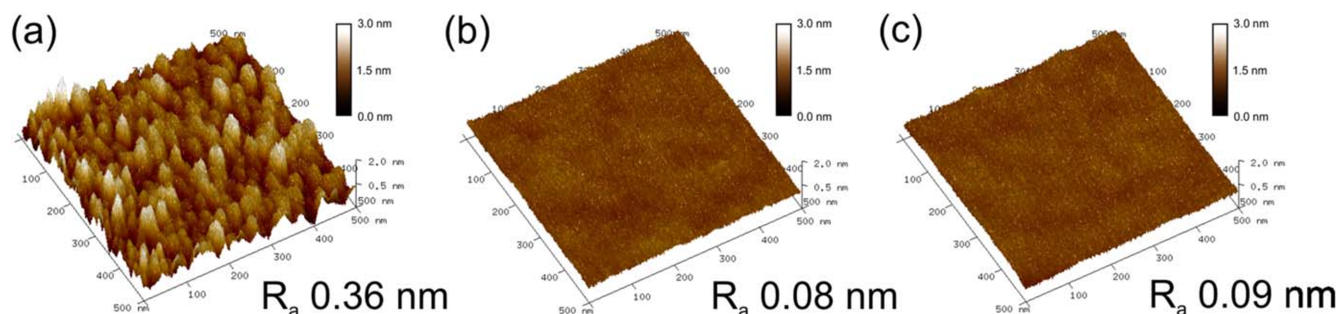

Figure 1. AFM images of the SiCN surface after (a) PDA, (b) CMP, and (c) N_2 plasma.

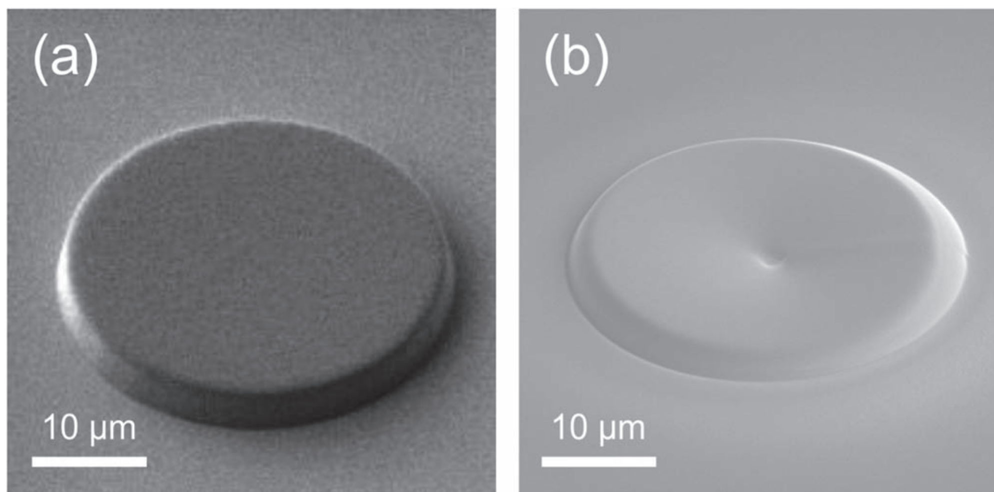

Figure 2. SEM images of (a) photo-patternable polymer and (b) W particle with a 25 μm diameter deposited on the bottom wafer.

velocity, the molecular mean free path, the air viscosity, and the wafer rigidity (Young's modulus and Poisson ratio).[41] Finally, Larrey et al. have experimentally confirmed the validity of the model. Therefore, there are two different measurements possible during wafer bonding, the adhesion energy to be considered during the bonding and the adherence energy to be considered after the bonding.

In-line SAM methodology using a 175 MHz transducer.—After the room temperature bonding and PBA, the bond uniformity and the presence of voids at the interface were inspected using in-line SAM metrology with a 175 MHz transducer. Figure 3 shows the SAM images of a bonded SiCN wafer pair with polymer particles at the bonding interface. In Fig. 3a, several visible white spots are visible related to the void formation induced by the polymer particles at the interface. Figure 3b show a magnified SAM image of the void induced by a polymer particle. For the 25 μm diameter polymer particles, the measured void size was approx. 700 μm in diameter. This means that the voids are over 30 times larger than the size of the particles. In addition, in Fig. 3b, several secondary voids were observed outward from the main void formed on 25 μm diameter polymer particles. This void tail was observed for all 25 μm diameter polymers and also for the W particles using a 175 MHz

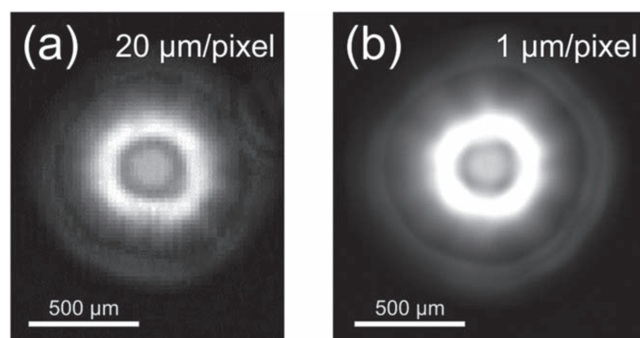

Figure 4. SAM images of the void induced by the 25 μm polymer particles with (a) 20 μm/pixel and (b) 1 μm pixel^{-1}.

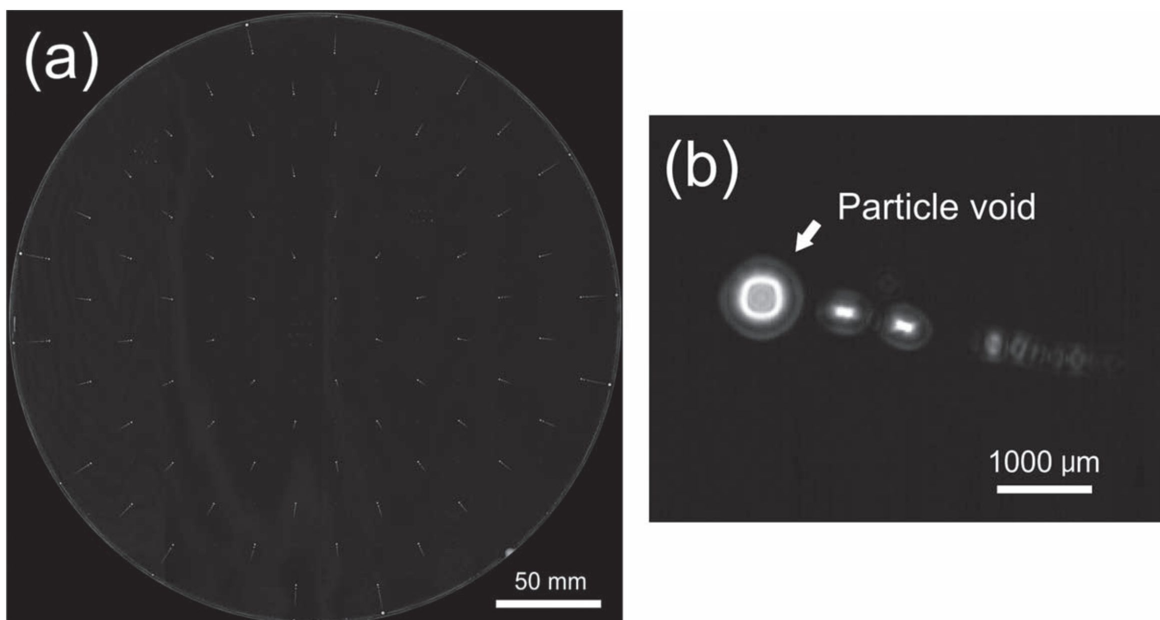

Figure 3. SAM images of bonded SiCN wafers after the room temperature bonding with polymer particles: (a) 300 mm full wafer and (b) magnified images of the void formation of 25 μm diameter particle. The gain parameter of 175 MHz transducers for 775 um top Si bonded wafer pairs is set as 30.

transducer. The properties and the formation mechanism of the void tail is discussed later.

A high-resolution scan using the 175 MHz transducer with a resolution of 1 μm pixel^{-1} was performed on the 25 μm polymer particle void to elucidate the void boundary. Here, the resolution in μm/pixel means the step length of one scan. Figure 4 shows SAM images of 25 μm polymer particle voids with a resolution of 20 μm pixel^{-1} and 1 μm pixel^{-1}. Although the scan resolution was increased from 20 μm pixel^{-1} to 1 μm pixel^{-1}, Figs. 4a and 4b show identical white area patterns since the resolution of reflected sound is controlled by the frequency emitted from the transducer. Consequently, with the 775 μm full-thickness Si, the SAM with the 175 MHz transducer is useful for a quick scan to visualize the bonding defects on the entire 300 mm diameter wafer. However, for a local scan of the sub-mm void, it is difficult to define the void boundary, i.e., the void size.

Manual SAM methodology at different frequencies.—The scan depth and the lateral (x–y) resolution (down to 1–10 μm) are dependent on the acoustic sound frequency emitted from the transducer. The SAM set-up can be equipped with transducers that generate ultrasonic waves ranging from 30 MHz to 1 GHz. The SAM images of the void formed on the 25 μm polymer particles scanned with different transducers using the manual SAM system (PVA Tepla, SAM300) are shown in Fig. 5. The gain parameter was tuned for each transducer to obtain a clear scanned image. By using a 30 MHz transducer (Fig. 5a), significant acoustic sound reflection (white areas) was obtained on the void. However, the detected tiny voids in the void tail show white areas overlapping with neighbouring voids due to low resolution, leading to an unclear definition of the void's boundary. When a higher frequency up to 175 MHz is used (Fig. 5d), a smaller white area was obtained, but the reflection of the acoustic sound was weaker than that detected using a lower frequency transducer. At low frequency a lower resolution but deeper sound penetration is expected. Thus, if the frequency increases, the resolution improves, but the high-frequency acoustic wave cannot travel deep in the material e.g., it is fully absorbed in the 775 μm full-thickness Si wafer. Therefore, to obtain a clear and precise SAM image with a 175 MHz or 400 MHz transducer, the top Si of the bonded wafer pair was first thinned down to 50 μm by a grinding process. SAM scans with 175 and 400 MHz transducers were then performed on the identical polymer particle voids. Figure 6 shows the SAM scan image of the polymer particle void under the 50 μm top Si scanned using 175 MHz and 400 MHz transducers. Thanks to the thinned top Si, a strong reflection signal for the 175 MHz transducer was detected, and the SAM image showed a clearer void boundary than that for the full-thickness top Si (Fig. 5d). Moreover, the SAM scan using the 400 MHz transducer provides an even more precise image of the void showing tiny voids invisible to the 175 MHz transducers (Fig. 6b). The 400 MHz transducer also allowed to detect cracks of the thinned top Si on the polymer particle void. This observed crack initiation relates to the Si thinning process was performed on the large void and is not a result of the bonding process. However, although the SAM scan using the 400 MHz transducer can define the void boundary clearly, the use of the 400 MHz transducer is technically limited for a full wafer scan because it requires a uniform top Si wafer. In addition, the focal length of the 400 MHz transducer has to be set below 500 μm by a manual handling operation. Based on that, the scan area is restricted to a small area, such as 5 mm × 5 mm, to prevent the 400 MHz transducers from scratching the sample surface. Because of these limitations, for practical purposes, the void size was defined using the SAM images obtained by the 175 MHz transducer available for full wafer scan with 775 μm full-thickness top Si.

Definition and calculation of void size.—To be able to define the void size using the in-line SAM image measured with the 175 MHz transducer, we need to correlate and calibrate by using the SAM image measured with the 400 MHz transducer. As shown in Fig. 6b, the SAM image obtained by the 400 MHz transducer provides a clearer void boundary definition. The methodology of the void size definition and calculation using the SAM image obtained by the 175 MHz transducer in combination with the SAM image of the 400 MHz transducer and image software ImageJ is shown in Fig. 7. First, one void on the SAM image of the 175 MHz transducer is selected. The diameter of each white circle in an image, e.g., binarized void, is calculated with a resolution of 20 μm pixel^{-1} to define the threshold of the color signal for the binarization in ImageJ. The threshold is specified as the binarized white area size that is equivalent to the void size obtained by the 400 MHz transducer. Based on that, binarization with the specified color threshold is applied to all SAM images captured by the 175 MHz transducer on a specific sample.

Results and Discussion

Characterization of particle voids after room temperature bonding.—As described in the experimental section, the adhesion energy should be considered for the void formation induced by particles. The adhesion energy for the SiCN wafer pair was measured using the opposite approach of the Maszara test, and a value of 51 mJ m^{-2} after 10 s and 67 mJ m^{-2} after 15 min was obtained. On the other hand, V. Larrey et al. has reported an adhesion energy of the SiO_2 bonded pair after plasma activation, from 81 to 108 mJ m^{-2}.[35] The adhesion energy is strongly dependent on the surface hydrophilicity and material roughness and surface finishing processes. In addition, the difference of measurement tool for the adhesion energy may give some variation of measured value. Comparing the adhesion energy value of the SiO_2 bonded pair reported by V. Larrey et al., the adhesion energy of 67 mJ m^{-2} for the SiCN wafer pair in this study is a reasonable value. Figure 8 shows the evolution of the void size induced by polymer and W particles as a function of particle position on the bonded SiCN wafer (see map in S1). The polymer and W particles with 25 μm diameters generate measured voids of approximately 650 μm and 750 μm of diameter, respectively. In other words, W particles generate measured voids 15% larger than those generated by polymer particles. The local change in the total thickness of the bonded wafer pair due to the particle presence was also investigated using patterned wafer geometry (PWG; KLA). Although the thickness of the as-deposited polymer particle is 2.6 μm, the analysis revealed a local increase in the total thickness of the bonded wafers of only 1.6 μm at areas where the polymer particles are present compared with the particle-free areas (Fig. S3). This means the polymer particle compressed 1.0 μm. For the W particles, little compression is assumed, but the PWG measurement could not be

Figure 5. SAM images on the void induced by the 25 μm polymer particle scanned by different transducers: (a) 30 MHz, (b) 50 MHz, (c) 100 MHz, and (d) 175 MHz under 775 μm full-thickness top Si. The void residue behind the partcle are observed. The gain parameter was tuned to obtain the clear qually for 30 MHz, 50 MHz, 100 MHz, and 175 MHz as 10, 10, 20, and 20, respectively.

Figure 6. SAM images of the void induced by the 25 μm polymer particle under the 50 μm top Si scanned by (a) 175 MHz and (b) 400 MHz transducers. The gain parameter under the 50 μm for 175 MHz and 400 MHz transducer are 20 and 40.

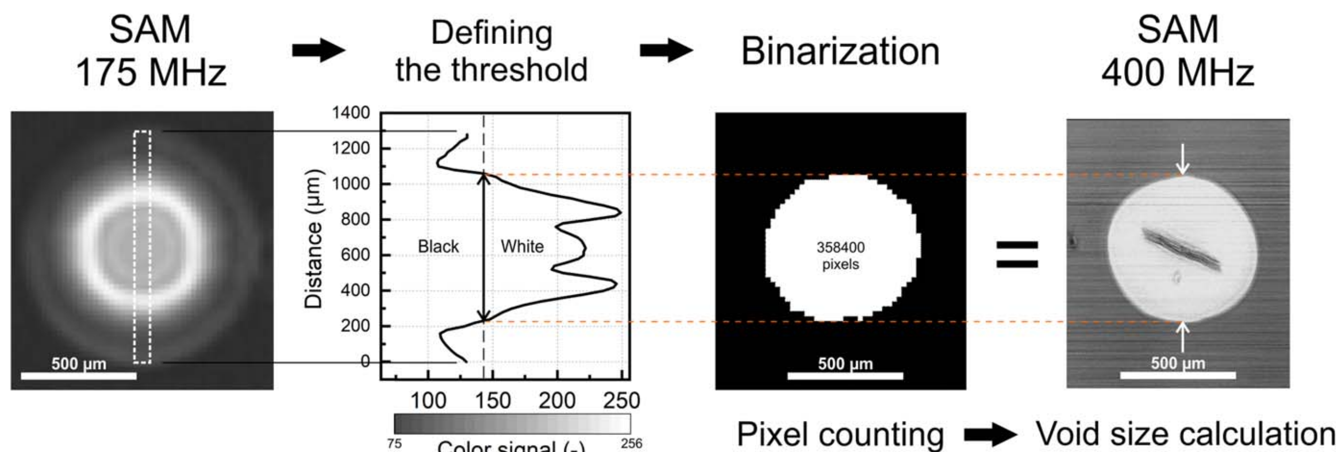

Figure 7. Process flow for the void size definition based on the SAM image obtained by the 175 MHz transducer through the combination of the SAM image of the 400 MHz transducer and image software ImageJ.

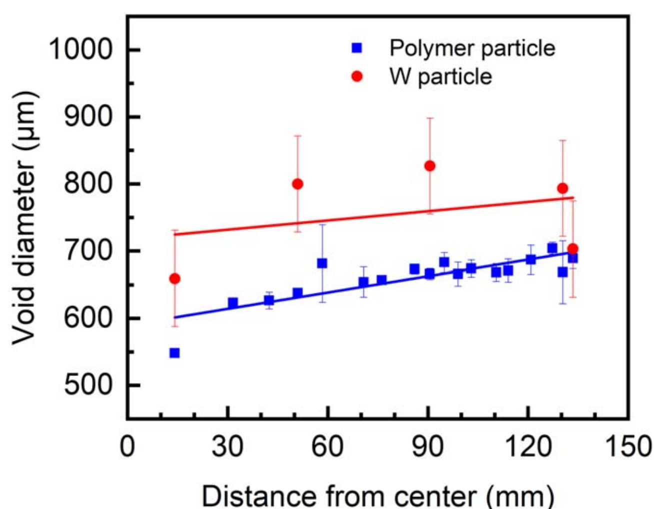

Figure 8. The void diameter induced by polymer and W particles of 25 μm diameters on each position of the SCN wafer, determined using the procedure described in section 2.5.

performed as the measurement set-up became unavailable. Instead, the deformation value of W particle was mathematically estimated based on the stress extracted from the deformation of polymer particle. Table I shows the Young's modulus of the photo-patternable polymer measured by material supplier and W particles.[42]

Table I. The Young's modulus of photo-patternable polymer and W particle, GPa

Photo-patternable polymer	2.2 ± 0.2
W	400 ± 11.0

Indeed, it is possible to calculate the stress applied on a particle by the action of two bonded wafers thanks to the Eq. 3 provided by H. J. Kim-Lee et al.:[30]

$$F = \sqrt{\frac{8\pi^2 \gamma E_w {t_w}^3}{3}} \quad [3]$$

In this analytical model, the force applied on the particle is expressed as function of the adhesion energy, wafers' thickness and rigidity. The force applied on the particles in the case of SiCN wafer having 67 mJ m^{-2} as adhesion energy, measured after 15 min, is calculated as 0.32 N. Hence, the stress applied on a particle with 25 μm of diameter is 0.65 GPa. This stress is significantly below the compression yield stress of pure W.[43,44] Therefore, Hooke's law $\sigma = E\varepsilon$, where σ is stress, E is Young's modulus, and ε is the strain ($\Delta h/h$), can be used to estimate the strain of W particles in the bonded wafers. The calculated strain of W particles' thickness resulting from 0.65 GPa of stress is around 0.16% which corresponds to 3.25 nm of thickness variation over 2 μm. The calculated strain of W particles using W bulk modulus and resulting from 0.65 GPa of stress, is around 0.16% which corresponds to 3.25 nm of thickness variation over 2 μm. However, Ishida et al.[45] reported the mechanical property of W particles deposited by FIB and measured a Young's modulus between 110 to 320 GPa depending on the deposition parameters. Compared to Young's modulus of W bulk, which is 400 GPa, the W deposited by FIB possesses the lower Young's modulus. Based on their observations, we could expect that the FIB deposition may also decrease the Young modulus of Pt particles compared to Pt bulk. Finally, if we assume that the W particle used in our study has a Young's modulus of 110 GPa, strain of the W particle under the applied stress 0.65 GPa is calculated as 0.59% which corresponds to 11.3 nm of thickness variation over 2 μm. In the case of a Young's modulus of 400 GPa the thickness variation should be around 3.3 nm. In both cases the deformation is pretty low.

Moreover, Q.-Y. Tong et al. has given the formula to predict the radius of the void induced by the particle in case that the adhesion energy, wafer thickness and rigidity parameter is known.[28,30,46] The

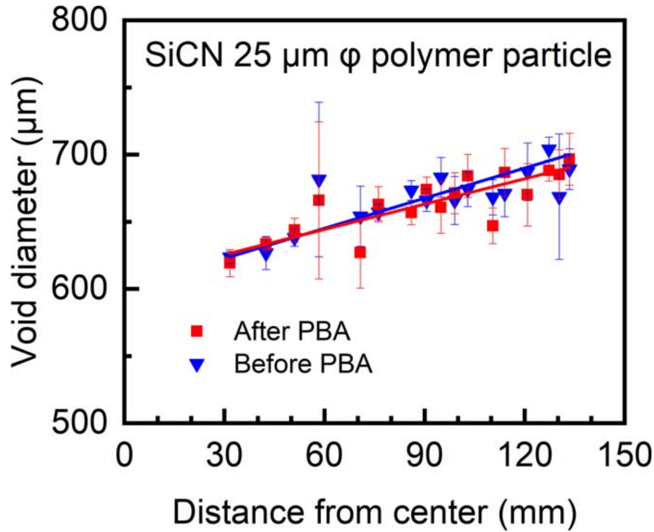

Figure 9. The void size of polymer particles of 25 μm diameters before and after PBA SiCN wafers.

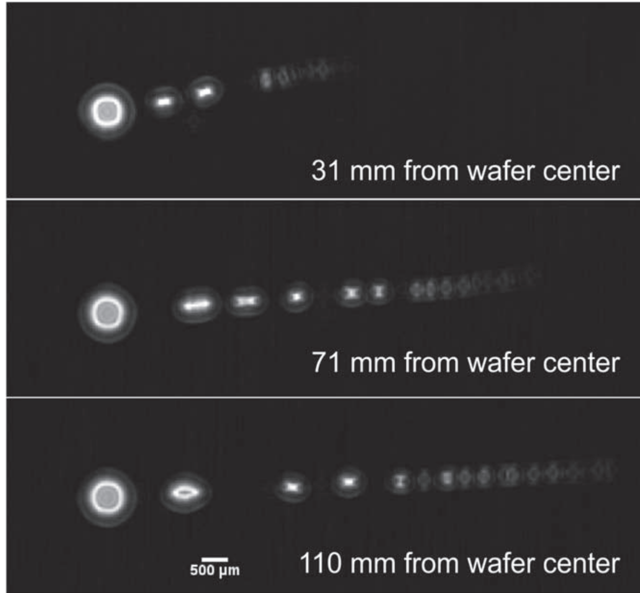

Figure 10. SAM images of polymer particles at three locations on the SiCN wafer.

formula is derived as:

$$R = \left[\frac{4}{3}\frac{E_{w1}t_{w1}{}^{3}E_{w2}t_{w2}{}^{3}}{\gamma(E_{w1}t_{w1}{}^{3} + E_{w2}t_{w2}{}^{3})}\right]^{1/4} h^{1/2} \quad [4]$$

where E_{w1} and E_{w2} are the Young's modulus of wafer 1 and 2 in Pa, t_{w1} and t_{w2} are the wafer thickness in mm, γ is the adhesion energy in J/m^2. In this study, identical wafers are used for the bonding. Hence, the formula can be simplified as:

$$R = \left(\frac{2}{3}\frac{E_w t_w{}^{3}}{\gamma}\right)^{1/4} h^{1/2} \quad [5]$$

Further, the radius R of the void induced by the particle is calculated as 6.7 mm (13.4 mm in diameter), which is around 20 times bigger than that we observed by SAM and IR microscope. However, the calculated radius of the void from the formula is the theoretical prediction and we did not observe such quite large voids formed on the polymer and W particle in this study. The difference between the radius of the void calculated by theoretical formula and observed in this study may be attributed to wafer bonding procedure, measurement sensitivity, and bond wave propagation in terms of fluid dynamics. These parameters are not considered in the theoretical calculation for the void radius. The origin of this difference should be investigated together with the computer simulation using fluid dynamics in the near future.

Furthermore, it was confirmed that the size of voids induced by particles increased when moving from the center of the wafer to the edge. This observation will be further discussed in the latter section related to the void tail formation and the bond wave propagation.

Characterization of particle voids after PBA.—To explore the impact of the annealing process on the void size, post bond annealing at 250 °C for 2 h is applied after bonding at room temperature. The bonding is clearly enhanced after the PBA under consideration. SAM inspection was also performed after PBA to observe the void size evolution. Figure 9 shows the evolution of the void size induced by the polymer particles obtained before and after PBA on SiCN wafer. Although the adherence energy of SiCN wafer measured by Maszara test was significantly increased after PBA (0.38 J m^{-2} to 2.32 J m^{-2}), the size of voids induced by polymer particles did not show any significant shrinkage at the micro-meter scale. Since the void defect occurs during the bonding, it is logical that the increase of the adherence energy after PBA measured by Maszara test does not result in the void size shrinkage. It also confirms that the measured void size is only impacted by the adhesion energy, i.e. the bond wave propagation. This result paves the way to the measurement of adhesion energy using particles which could allow to obtain adhesion energy maps instead of a unique value at the wafer edge. In addition, FTIR analysis on the particle void including the polymer and W particle was performed to compare the components in the polymer particle and W particle void

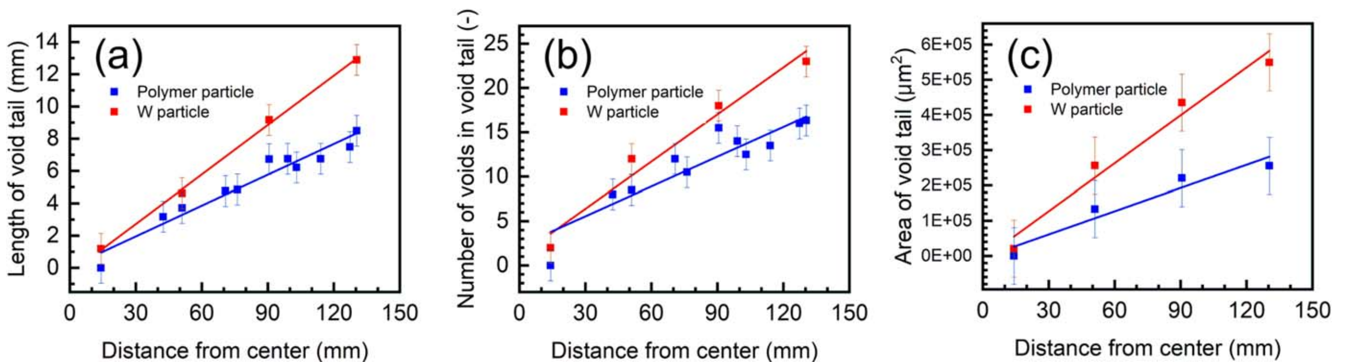

Figure 11. Void tail properties of polymer and W particles on the SiCN wafer: (a) length of void tail, (b) number of voids in void tail, and (c) total area of void tail versus its distance from the wafer center.

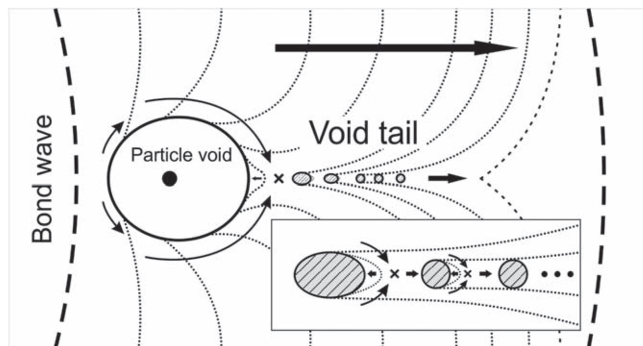

Figure 12. Schematics of voids and void tail formation impacted by bond wave propagation.

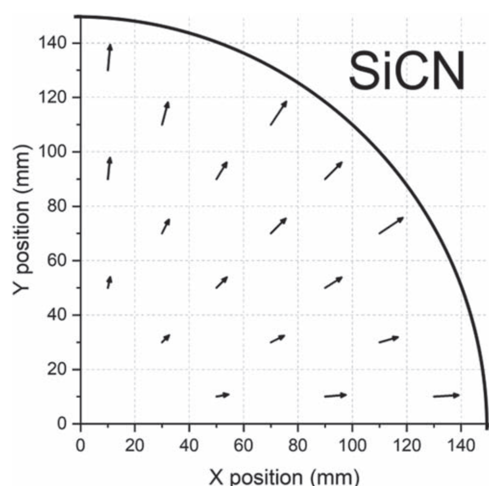

Figure 13. The direction and length of the void tail behind the 25 *u*m diameter polymer particles on the quarter wafer. The length of arrows corresponds to the length of the void tail in mm.

before and after PBA. No changes of the FTIR spectra between before and after PBA was confirmed, meaning no/little impacts of the decomposition neither of the polymer and W particle.

Characterization of void tails after room temperature bonding.—As shown before in Fig. 2b, using a 175 MHz transducer, it is possible to observe a series of voids of smaller diameter behind the main void. This series is called the void tail. Depending on the particle's position on the wafer, the characteristics of the particle void and the void tail, such as the length and the number of secondary voids, differ as shown in Fig. 10. Indeed, one can observe from the SAM images that the length and number of voids in the void tail increase as a function of the distance from the wafer's center. As shown in Fig. 11, a comparison of the void tail characteristics induced by polymer and W particles on the bonded wafers has also been done. As the distance from the center increases, W particles generate a longer void tail and a larger number of secondary voids. It is also worth noting that the void tail characteristics can be correlated with the size of the main void; the larger the main void, the longer the void tail. These observations would be consistent with the assumption of an included volume of air that propagates away from the main physical void.

The relationship between radial position of the particle (and main void) and void tail can be attributed to the fact that large particles cause a considerable deviation in the bond wave, i.e., the difference in the bond wave velocity and configuration. In our experiments, the bonding is realized at room temperature and initiated from the wafer's center. The bond wave then propagates to the edge concentrically due to pressure-free bonding. We propose that the void tail formation is caused by a change in the bond wave propagation around the particle. E. Navarro has reported the recording (photoshoots every 1 s) of a bond wave propagation around the particle resulting in void formation on the particle and void bubble group (called void tail in this study) formed behind a particle void.[47] This observation explains dynamics and mechanism of the bond wave propagation around the particle forming the particle void and void tail. Therefore, based on the observation of E. Navarro, the assumed formation mechanism of the particle void and void tail is schematically described in Fig. 12. One would keep in mind that the defect sizes measured in our case is much lower than the one measured by Navarro et al. Therefore, the dynamics could be slightly different. In fact, it has been reported that when two bond wavefronts meet each other, it results in the creation of a void.[32,45] When the bond wave propagating from the wafer center encounters the particle, it locally slows down and creates two split waves. These two waves propagate around the particle slowly and enclose the particle together with residual air, resulting in the main void formation. Moreover, the bond wave that did not hit the particle propagates faster than the retarded waves. Once two waves running around the particle merge behind the particle, the merged bond wave drags the rest of the air separated from the main void forward. Then before the residual air rejoins the front line, the bond wave merges again in front of the residual frontward pushed air.[46] If the speed difference between the bond wave retarded by residual air and the bond wave running far from the particle becomes larger, the number of air bubbles increases and appears over a longer distance. These air bubbles results in the void tail formation. We therefore suggest that the bond wave governs the appearance of void tails.

Previous studies[33,41,48] determined that the bond wave is governed by a dynamic balance between the driving force of the bonding, the air evacuation in the narrow gap between the two wafers, and the elastic deformation of the wafer. The airflow dynamics are different between the wafer center and the wafer edge, due to the different amount of air to be evacuated and therefore the velocity of the bond wave might also differ. V. Dragoi et al., have reported that the bond wave propagation is not uniform between the wafer center and edge, i.e. it moves faster at the wafer edge than at the wafer center.[32,41] Moreover, in our study the bond wave starting from the wafer center experiences multiple obstacles while propagating: when it hits the particle, it creates two bond fronts that merge again behind the particle. This means that the bond wave may run at a different velocity, expected to slow down, compared to the single bond wave. This slow-downed bond wave may hit the next particle where it creates larger particle void and longer void tail compared to those of previous particle. The difference of the bond wave velocity between the wafer center and edge can be also attributed to the mechanical deformation of the top wafer which is not the same at the center than near the edge. Figure 13 shows the direction and length of the void tails behind the polymer particles on a quarter SiCN wafer, assuming undisturbed movement. In Fig. 13, the length of the arrows indicates the length of the void tail in mm, and the arrows show the directions of the void tails outwards from the wafer center (0,0). The void tail is stretching longer at the wafer edge. Furthermore, the size of main voids induced by particles increased with going to the wafer edge as shown in Fig. 8. Regarding the particle void and void tail formation, we propose that if the bond wave is slower at the wafer center, the main void will be smaller, and the void tail will be shorter because the particle will have less of an impact on the bond wave velocity near the wafer center.

To study further the nature of the void tail formation, twelve W particles were deposited on the SiCN wafer with increasing distances between particles in line; for example, a distance of 1.4 mm between the first and second W particles, and 2.8 mm between the second and third W particles (Fig. S4). Figure 14 shows the SAM images of the void formation along with the line of W particles. Interestingly, in Fig. 14b, the first, second, and third particle voids have formed only one large void. This is due to the small distance between each

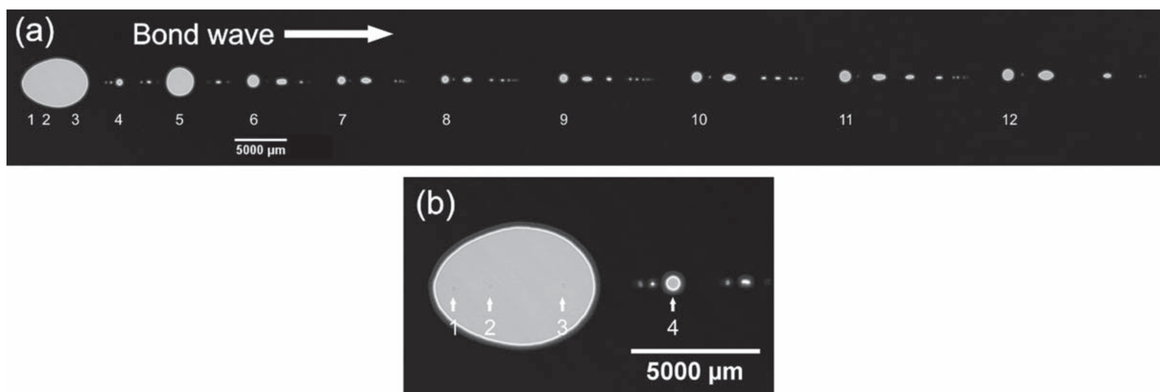

Figure 14. SAM images of the void formation induced by twelve W particles deposited with increasing distance between each particle in one line (Fig. S4), (a) void formations of all W particles, (b) magnified SAM image from first and fourth W particle.

particle, which impedes the bond wave recombination before reaching the next particle. The first W particle in this deposition scheme is positioned 31.1 mm from the wafer center, and the distance between the first and second particle is 1.4 mm. Furthermore, the position of the second W particle is 32.5 mm, and the distance between this particle and the third particle is 2.8 mm. These distances between W particles are equivalent to or shorter than the estimated length of the void tails of W particles. This result clearly shows that several voids can possibly combine to form a large void if the distance between particles is shorter than the length of the void tail. This recombination is of great interest in hybrid bonding applications involving a fine-pitch interconnect layout if the misaligned or over-protruded Cu pads used in hybrid bonding scheme are 'obstructing' the bonding interface, the bonding tail will repeat itself, leading to the formation of huge voids on these misaligned areas. It is also noteworthy that if the mislanded Cu pad stands higher, the voids tails should be longer.

Correlation between bond wave and edge void.—In wafer-to-wafer direct bonding, we have confirmed that the void forming at the wafer edge, −3.0 mm inside from the wafer outermost, (i.e., the edge void) appeared during bonding at room temperature. The edge void leads to a critical risk of rim chipping during the edge trimming process. Figure 15 shows SAM images focused on the edge of SiCN wafers without any particles (Fig. 15a) and with polymer particles located near the wafer edge (Fig. 15b). As shown in Fig. 15a, the edge void is formed on the full rim of the wafer. It has been reported earlier that the edge void is related to water droplets condensation due to air adiabatic depressurization.[33] However, interestingly, behind the void tail induced by polymer particle located near the wafer edge, the edge void was formed larger than the normal edge void as shown in Fig. 15b. The bond wave around the void tail propagates in a different manner (Fig. 12 right zone) than the normal bond wave starting from the wafer's center. If the particle is located relatively close to the wafer's edge, the bond wave may reach the wafer's edge as two wavefronts. Then these two wavefronts push the air in gap faster and the water condensation occurs more significantly than that of single bond wave. Hence, the water droplet condensation by two wavefronts remains at the wafer edge as a larger edge void.

To further understand the correlation between the bond wave and the formation of edge voids, W particles were deposited closer to the edges of SiCN wafers. Figure 16 shows the SAM image of void formation induced by a W particle at the wafer edge and a schematic drawing illustrating the pathway of the bond wave. The edge void is not observed behind the W particle located closer to the wafer edge, whereas the main void induced by the W particle is formed over three times bigger than that located at the center side. Thus, it is considered that the particle void combines with the void tail because the two wavefronts propagate vertically against the wafer edge after it passes the W particle and pushes the air back toward the particle void as shown in Fig. 16b. In the past study, the edge void was not visible if the bond wave runs vertically to the wafer edge.[33] Based on this potential mechanism, we can indirectly assume that no edge

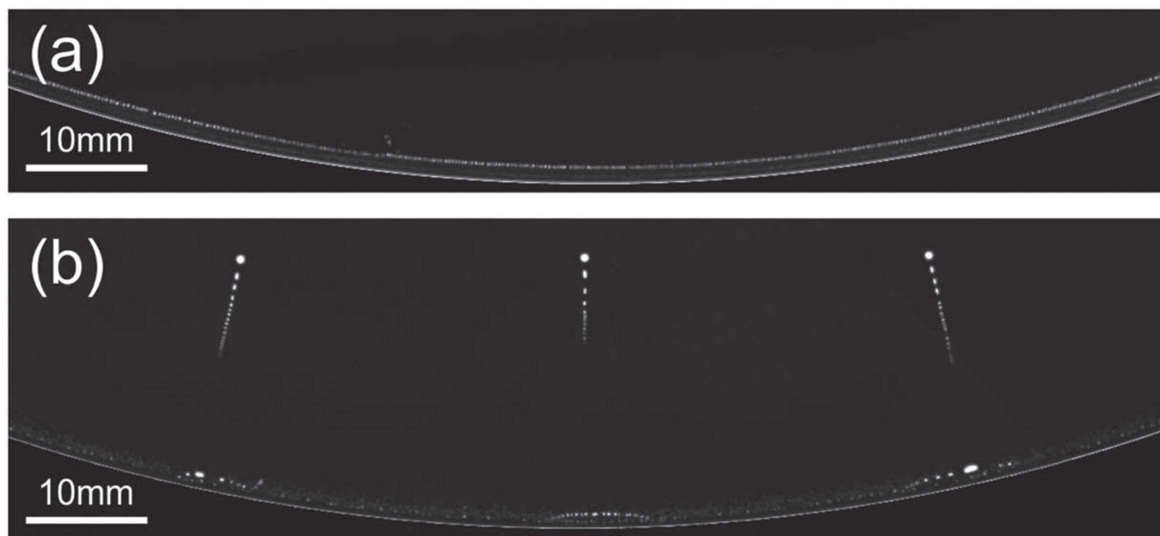

Figure 15. SAM images focused on the edge of SiCN wafers (a) without any particles and (b) with polymer particles located near the wafer edge.

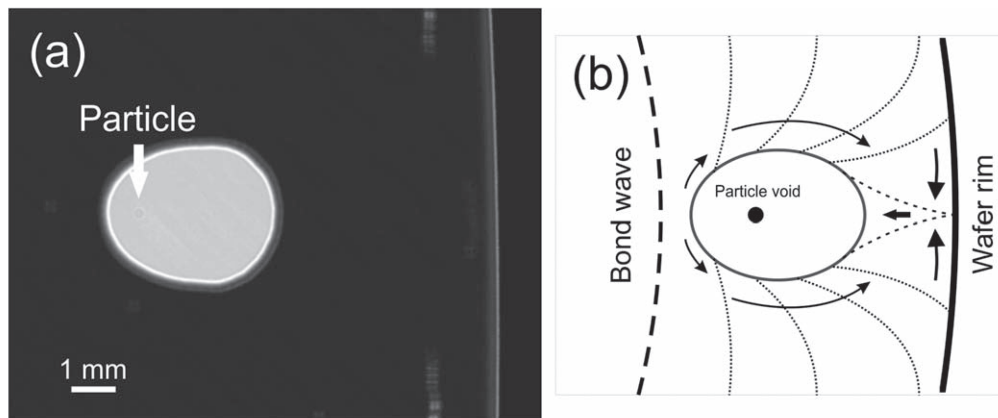

Figure 16. (a) SAM image of void formation induced by a W particle at the wafer edge and (b) schematic drawing indicating the path of the bond wave.

void formation behind the W particle shown in Fig. 16a might be assigned to the less or no water droplet condensation due to less effect of air adiabatic depressurization by the bond wave running vertically to the wafer edge. If the bonding is initiated at the wafer edge, we expect the edge void to form less than if the bonding starts from the wafer center. Also, the bond wave speed right behind the W particle is considered to be slow enough not to cause adiabatic depressurization of the air causing the edge void. On the other hand, the bigger edge void formed in an arch shape was observed as shown in Fig. 15b. This is considered that a faster bonding wave pulled by the bonding wave far away from the defect (the bond wave like Fig. 12 right side) reached to the wafer edge and formed the edge void in an arch shape. However, direct bonding from the wafer's edge remains a significant technical challenge in the bonding alignment process. Monitoring the bond wave velocity and propagation is of tremendous interest to control the void formation in wafer-to-wafer direct bonding. The correlation between the void formation and the bond wave propagation should be quantitatively studied with a specific room temperature bonding sequence in the near future.

Conclusions

The physical void formation induced by polymer and W particles was investigated to study its impact on the wafer-to-wafer bonding interface with the SiCN layer. In general, the measured diameter of the voids largely exceeds the dimensions of the particles, i.e. the voids for the 25 μm diameter polymer and W particles were estimated to be 700 μm, respectively. The W particles formed larger voids than the polymer particles because of the particle height. Although the adherence energy was increased significantly by PBA, the void size remained unchanged for the SiCN wafer postulated as not the adherence energy measured by Maszara test but the adhesion energy should be considered when the bonding and the void defect occur. In addition, void tails were observed behind the 25 μm diameter polymer and W particles using a 175 MHz transducer. The void tails became longer and the number of voids in a void tail increased with increasing distance from the wafer center and was also more pronounced for the W particle induced voids. Based on the observations analyzed in this study and previous reports, the bond wave propagation was verified as one of the main factors contributing to the differences in properties of voids and void tails depending on the particle positions. Additionally, it was determined that the void tail property is related to the size of the front particle void. The combined void reproduced the importance to improve the hybrid bonding scheme as failure cases such as misalignment or over-protruded Cu pad. The correlation between the void tail and edge void was studied based on a W particle deposited at the wafer edge. It was revealed that the edge void was a by-product, water droplet condensation, induced by bond wave propagation from the wafer center.

Acknowledgments

The authors acknowledge imec's 3D team for valuable input.

ORCID

F. Nagano https://orcid.org/0000-0001-5315-8694

References

1. E. Beyne, *IEEE Design & Test*, **33**, 8 (2016).
2. M. Ohyama, M. Nimura, J. Mizuno, S. Shoji, M. Tamura, T. Enomoto, and A. Shigetou, *2015 IEEE Electronic Components and Technology Conference*, p. 325 (2014).
3. P. Batude et al., *2014 IEEE Int. Interconnect Technol. Conf. (IITC)*, p. 373 (2014).
4. F. Inoue, J. Derakhshandeh, M. Lofrano, and E. Beyne, *Jpn. J. Appl. Phys.*, **60**, 026502 (2021).
5. T. Tabata, L. Sanchez, V. Larrey, F. Fournel, and H. Moriceau, *Microelectron. Reliab.*, **107**, 113589 (2020).
6. R. Tadepalli, K. T. Turner, and C. V. Thompson, *Acta Mater.*, **56**, 438 (2008).
7. B. Lee, H. Jeon, K. W. Kwon, and H. J. Lee, *Acta Mater.*, **61**, 6736 (2013).
8. J. Utsumi and R. Takigawa, *Scr. Mater.*, **191**, 215 (2021).
9. T. Matsumae, Y. Kurashima, H. Takagi, H. Umezawa, and E. Higurashi, *Scr. Mater.*, **191**, 52 (2021).
10. V. Dragoi, G. Mittendorfer, C. Thanner, and P. Lindner, *Microsyst. Technol.*, **14**, 509 (2008).
11. F. Inoue et al., *ECS J. Solid State Sci. Technol.*, **8**346 (2019).
12. J. Utsumi, K. Ide, and Y. Ichiyanagi, *Micro Nano Eng.*, **2**, 1 (2019).
13. C. T Ko and K. N Chen, *Microelectron. Rel.*, **52**, 302 (2012).
14. F. Mu, K. Iguchi, H. Nakazawa, Y. Takahashi, M. Fujino, R. He, and T. Suga, *Appl. Phys. Express*, **9**, 081302 (2016).
15. S. Kim, L. Peng, A. Miller, G. Beyer, E. Beyne, and C. Lee, *2015 International 3D Systems Integration Conference (3D-IC), TS7.2.* (2015).
16. E. Beyne et al., *2017 IEEE International Electron Devices Meeting (IEDM)*, p. 32.4.1 (2017).
17. F. Inoue, S. Iacovo, Z. E. Mekki, S. W. Kim, H. Struyf, and E. Beyne, *IEEE Electron Device Lett.*, **42**, 1826 (2021).
18. S. Iacovo, L. Pemg, A. Phommahaxay, F. Inoue, P. Verdonck, S. W. Kim, E. Sleeckx, A. Miller, F. Beyer, and E. Beyne, *2019 IEEE Electronic Components and Technology Conference (ECTC)*, p. 2206 (2019).
19. C. Ventosa, C. Morales, L. Libralesso, F. Fournel, A. M. Papon, D. Lafond, H. Moriceau, J. D. Penot, and F. Rieutord, *Electrochem. Solid-State Lett.*, **12**, H373 (2009).
20. C. Ventosa, F. Rieutord, L. Libralesso, C. Morales, F. Fournel, and H. Moriceau, *J. Appl. Phys.*, **104**, 123524 (2008).
21. R. Stengl, T. Tan, and U. Gösele, *Jpn. J. Appl. Phys.*, **28**, 1735 (1989).
22. T. Plach, K. Hingerl, S. Tollabimazraehno, G. Hesser, V. Dragoi, and M. Wimplinger, *J. Appl. Phys.*, **113**, 094905 (2013).
23. F. Fournel, C. Martin-Cocher, D. Radisson, V. Larrey, E. Beche, C. Morales, P. A. Delean, F. Rieutord, and H. Moriceau, *ECS J. Solid State Sci. Technol.*, **4**, P124 (2015).
24. F. Nagano et al., *ECS J. Solid State Sci. Technol.*, **9**, 123011 (2020).
25. L. Peng et al., *2018 IEEE Int. Interconnect Technol. Conf. (IITC)*, p. 179 (2018).
26. C. Wang, Y. Liu, and T. Suga, *ECS J. Solid State Sci. Technol.*, **6** (2017).
27. A. Plößl and G. Kräuter, *Mater. Sci. Eng.*, **R25**, 1 (1999).
28. U. Gösele and Q. Y. Tong, *Annu. Rev. Mater. Sci.*, **28**, 215 (1998).
29. H. J. Kim-Lee, A. Kim, D. Kim, J. Jeon, K. Woo, and B. Park, *ECS Trans.*, **50** (2012).
30. C. Wang, Y. Liu, Y. Li, Y. Tian, C. Wang, and T. Suga, *ECS J. Solid State Sci. Technol.*, **6**, 373 (2017).
31. V. Dragoi, P. Czurratis, S. Brand, J. Beyersdorfer, C. Patzig, J. P. Krugers, F. Schrank, J. Siegert, and M. Petzold, *ECS Trans.*, **50**, 227 (2012).

32. A. Castex, M. Broekaart, F. Rieutord, K. Landry, and C. Lagahe-Blanchard, *ECS Solid State Lett.*, **2**, 47 (2013).
33. D. Grierson and K. T. Turner, *ECS Trans.*, **33**, 573 (2010).
34. V. Larrey, G. Mauguen, F. Fournel, D. Radisson, F. Rieutord, C. Morales, C. Bridoux, and H. Moriceau, *ECS Trans.*, **75**, 145 (2016).
35. W. P. Maszara, G. Goetz, A. Caviglia, and J. B. McKitterick, *J. Appl. Phys.*, **64**, 4943 (1998).
36. T. Martini, J. Steinkirchner, and U. Gösele, *J. Electrochem. Soc.*, **144**, 354 (1997).
37. Y. Bertholet, F. Iker, J. P. Raskin, and T. Pardoen, *Sens. Actuator A Phys.*, **110**, 157 (2004).
38. D. Pasquariello and K. Hjort, *J. Electrochem. Soc.*, **147**, 2343 (2000).
39. K. T. Turner and S. M. Spearing, *J. Appl. Phys.*, **103**, 013514 (2008).
40. F. Rieutord, B. Bataillou, and H. Moriceau, *Phys. Rev. Lett.*, **94**, 236101 (2005).
41. G. P. Škoro, J. R. J. Bennett, T. R. Edgecock, S. A. Gray, A. J. McFarland, C. N. Booth, K. J. Rodgers, and J. J. Back, *J. Nucl. Mater.*, **409** (2011).
42. A. M. Lennon and K. T. Ramesh, *Mater. Sci. Eng. A*, **276**, 9 (2000).
43. J. Y. Kim, D. Jang, and J. R. Greer, *Acta Mater.*, **58**, 2355 (2010).
44. M. Ishida, J. Fujita, T. Ichihashi, Y. Ochiai, T. Kaito, and S. Matsui, *J. Vac. Sci. Technol. B Microelectron. Nanom. Struct.*, **21**, 2728 (2003).
45. Q.-Y. Tong and U. Gösele, *Semiconductor Wafer Bonding: Science and Technology* (Wiley, New York) (1998).
46. E Navarro, (2014), English. ⟨tel-01048574v1⟩Direct Wafer Bonding Dynamics. Mechanics [physics.med-ph].Université de Grenoblehttps://tel.archives-ouvertes.fr/tel-01048574v1.
47. S. Bengtsson, K. Ljungberg, and J. Vedde, *Appl. Phys. Lett.*, **69**, 3381 (1996).
48. C. Sabbione, L. Di Cioccio, L. Vandroux, J.-P. Nieto, and F. Rieutord, *J. Appl. Phys.*, **112**, 063501 (2012).